



Effects of skeleton structure on necrosis targeting and clearance properties of radioiodinated dianthrones

Dongjian Zhang, Cuihua Jiang, Shengwei Yang, Meng Gao, Dejian Huang, Xiaoning Wang, Haibo Shao, Yuanbo Feng, Ziping Sun, Yicheng Ni, Jian Zhang & Zhiqi Yin

To cite this article: Dongjian Zhang, Cuihua Jiang, Shengwei Yang, Meng Gao, Dejian Huang, Xiaoning Wang, Haibo Shao, Yuanbo Feng, Ziping Sun, Yicheng Ni, Jian Zhang & Zhiqi Yin (2015): Effects of skeleton structure on necrosis targeting and clearance properties of radioiodinated dianthrones, Journal of Drug Targeting, DOI: [10.3109/1061186X.2015.1113541](https://doi.org/10.3109/1061186X.2015.1113541)

To link to this article: <http://dx.doi.org/10.3109/1061186X.2015.1113541>

 View supplementary material [↗](#)

 Published online: 19 Nov 2015.

 Submit your article to this journal [↗](#)

 Article views: 9

 View related articles [↗](#)

 View Crossmark data [↗](#)

ORIGINAL ARTICLE

Effects of skeleton structure on necrosis targeting and clearance properties of radioiodinated dianthrone

Dongjian Zhang^{1,2}, Cuihua Jiang¹, Shengwei Yang¹, Meng Gao¹, Dejian Huang¹, Xiaoning Wang¹, Haibo Shao³, Yuanbo Feng^{1,5}, Ziping Sun⁴, Yicheng Ni^{1,4,5}, Jian Zhang¹, and Zhiqi Yin²¹Laboratory of Translational Medicine, Jiangsu Province Academy of Traditional Chinese Medicine, Nanjing, Jiangsu Province, P.R. China,²Department of Natural Medicinal Chemistry & State Key Laboratory of Natural Medicines, China Pharmaceutical University, Nanjing, Jiangsu Province, P.R. China, ³Department of Radiology, the First Affiliated Hospital of China Medical University, Shenyang, Liaoning Province, P.R. China,⁴Radiation Medical Institute, Shandong Academy of Medical Sciences, Jinan, Shandong Province, P.R. China, and ⁵Theragnostic Laboratory, Campus Gasthuisberg, KU Leuven, Leuven, Belgium

Abstract

Necrosis avid agents (NAAs) can be used for diagnose of necrosis-related diseases, evaluation of therapeutic responses and targeted therapeutics of tumor. In order to probe into the effects of molecular skeleton structure on necrosis targeting and clearance properties of radioiodinated dianthrone, four dianthrone compounds with the same substituents but different skeletal structures, namely Hypericin (Hyp), protohypericin (ProHyp), emodin dianthrone mesomer (ED-1) and emodin dianthrone raceme (ED-2) were synthesized and radioiodinated. Then radioiodinated dianthrone were evaluated *in vitro* for their necrosis avidity in A549 lung cancer cells untreated and treated with H₂O₂. Their biodistribution and pharmacokinetic properties were determined in rat models of induced necrosis. *In vitro* cell assay revealed that destruction of rigid skeleton structure dramatically reduced their necrosis targeting ability. Animal studies demonstrated that destruction of rigid skeleton structure dramatically reduced the necrotic tissue uptake and speed up the clearance from the most normal tissues for the studied compounds. Among these ¹³¹I-dianthrone, ¹³¹I-Hyp exhibited the highest uptake and persistent retention in necrotic tissues. Hepatic infarction could be clearly visualized by SPECT/CT using ¹³¹I-Hyp as an imaging probe. The results suggest that the skeleton structure of Hyp is the lead structure for further structure optimization of this class of NAAs.

Keywords

Autoradiography, biodistribution, necrosis targeting, pharmacokinetics, radioiodinated dianthrone, SPECT/CT imaging

History

Received 18 July 2015

Revised 12 October 2015

Accepted 25 October 2015

Published online 20 November 2015

Introduction

Necrosis represents a principal feature of numerous pathologies or disorders such as ischemic cardiac disease, atherosclerosis, stroke, sepsis, pancreatitis and malignant tumors [1,2]. It is often classified as an uncontrolled, accidental process of cell or tissue death that results from chemical or physical noxious insults and ischemic or inflammatory injury [3]. Differing from apoptosis, necrosis usually involves groups of cells and is frequently followed by granulation development and fibrosis replacement with distortion of the local tissue's architecture [4–6]. Thus the presence of necrotic tissue may provide an anchorage for the diagnosis, prognosis or treatment of aforementioned diseases. Necrosis avid agents

(NAAs) are a class of compounds that selectively concentrate in the necrotic tissue after systemic administration, which can be used for *in vivo* imaging of necrotic tissue [3,7] and tumor necrosis therapy (TNT) [8–12].

A common strategy for effective molecular imaging and targeted therapeutics is to employ a suitably designed molecular probe that is composed of a targeting group conjugated to a reporter group or therapeutic group. A number of molecular probes with high avidity for necrotic tissue have been explored for diagnosis and treatment of necrosis-related pathologies such as ^{99m}Tc-pyrophosphate [13], ^{99m}Tc-glucuronate [14–16], ¹¹¹In-antimyosin monoclonal antibody [17,18], ¹²³I-hypericin monocarboxylic acid (¹²³I-HMA) [19], ^{99m}Tc(CO)₃-bis-DTPA-pamoate [20], ¹²³I/¹³¹I-hypericin(¹²³I/¹³¹I-Hyp) [21,22], Hoechst-IR [1] and ⁶⁴Cu-bis-DOTA-Hyp [23], etc. Among them, the most studied is Hyp. ¹²³I-Hyp allowed visualization of necrotic tissue and may serve as a potential necrosis-avid diagnostic agent for assessment of tissue viability [24–27]. ¹³¹I-Hyp has been explored for diagnostic and therapeutic utilities in experimental malignancies [8,10,11]. The inherent fluorescence properties of Hyp have also been exploited for

Address for correspondence: Dr. Jian Zhang, Laboratory of Translational Medicine, Jiangsu Province Academy of Traditional Chinese Medicine, No. 100, Shizi Street, Hongshan Road, Nanjing 210028, Jiangsu Province, P.R. China. Tel: +86 25 52362107. E-mail: zjwonderful@hotmail.com; Dr. Zhiqi Yin, Department of Natural Medicinal Chemistry & State Key Laboratory of Natural Medicines, China Pharmaceutical University, No. 24, Tongjiyaxiang, Gulou District, Nanjing 210009, Jiangsu Province, P.R. China. Tel: +86 25 86185371. E-mail: chyq2005@126.com

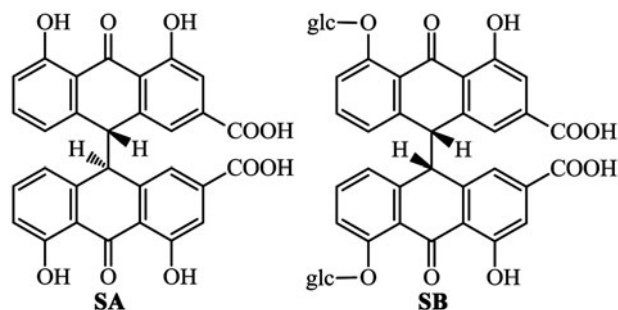


Figure 1. The chemical structures of sennidin A (SA) and sennoside B (SB), glc = β -D-glucopyranosyl.

microscopic necrosis imaging [28,29]. However, Hyp is a lipophilic compound that sparingly dissolves and forms aggregates in aqueous solution [30]. It makes systemic administration problematic and, in turn, reduces its biodistribution to necrotic tissue and shows unwanted biodistribution in normal tissue [31,32].

In recent years, we have committed to discover new necrosis avid probes for noninvasive imaging diagnosis of necrosis-related pathologies and dual-targeting theragnostic strategy of tumors. In addition to Hyp, we found that median dianthrone compounds sennidin A (SA) [12] and sennoside B (SB) [33] (Figure 1) also had necrosis targetability. Compared with Hyp, SA and SB both have better water solubility and giant π -conjugation damaged parent nucleus structure. The fewer uptakes of ^{131}I -SA and ^{131}I -SB in the lung compared with ^{131}I -Hyp suggested that SA and SB may be prone to aggregation to a lesser degree than Hyp.

Although dianthrone compounds, Hyp, HMA, SA and SB all reveal necrosis targeting property, the necrosis targeting ability of them is different. This is mainly due to the difference of their parent nucleus structures and their peripheral substituents. To seek for new necrosis targeting compounds and to provide the basis for further structural optimization, we decided to first explore the effects of skeleton structure on necrosis targeting and clearance properties of radioiodinated dianthrones. Therefore, we synthesized four dianthrone compounds with the same substituents but different skeletal structures, namely Hyp, protohypericin (ProHyp), emodin dianthrone mesomer (ED-1) and emodin dianthrone raceme (ED-2) (Figure 2). After radioiodination, necrosis targeting and pharmacokinetic properties of the four ^{131}I -dianthrones were examined in rat models with reperfused partial liver infarction (RPLI) and absolute ethanol induced muscular necrosis. Thereafter, we further evaluated the ability of ^{131}I -Hyp to image necrosis *in vivo* in rats with RPLI.

Materials and methods

Chemistry

All reagents and solvents used, unless stated otherwise, were purchased from Sinopharm Chemical Reagent Co., Ltd or Nanjing Chemical Reagent Co., Ltd (Nanjing, China) and were used without further purification. The starting material emodin was purchased (Chengdu Huaxia Chemical Reagent Co., Ltd, Chengdu, China). Sodium iodide (Na^{131}I) was supplied by HTA Co., Ltd (Beijing, China). The radioactivity

concentration was 370 MBq/mL and the radionuclidic purity was greater than 99%. Thin layer chromatography (TLC) was performed on Merck aluminum-precoated silica gel 60 F₂₅₄ plates or Silica gel 60 RP-18 F₂₅₄ plates with spots visualized by UV light (254 nm or 365 nm) and/or by development with magnesium acetate, or aluminum chloride. Column chromatography was carried out with Merck silica gel 60 normal phase (45–75 μm) or Sephadex LH20. ^1H NMR was recorded on a Bruker 300 or 500 MHz spectrometer and ^{13}C NMR spectra were recorded at 75 MHz. Chemical shifts are reported as parts per million (δ) relative to tetramethylsilane (TMS, 0.00 ppm), which was used as an internal standard. MS spectra were measured by HP1100 mass spectrometer utilizing electrospray ionization (ESI) (Agilent, Santa Clara, CA).

Synthesis of emodin anthrone

Emodin anthrone was synthesized following a literature procedure [34] with slight modification. A solution of tin (II) chloride hydrate (29.1 g, 129 mmol) in conc. hydrochloric acid (149 mL) was added to a suspension of emodin (3.49 g, 12.9 mmol) in acetic acid (270 mL) to give the red-colored solution. After the solution was stirred at 120 °C for 24 h, it was poured into 1000 mL of ice-water and the precipitate was collected by filtration and dried *in vacuo* at 60 °C to give 1 (3.2 g, 96.9%). The resulting emodin anthrone was directly used in the next reaction without further purification.

Synthesis of ProHyp

ProHyp (1.25 g, 63.2%) was synthesized following a literature protocol [35] and purified by preparative reversed phase-high performance liquid chromatography (RP-HPLC) (see Supplementary data). Data for ProHyp: ^1H NMR (300 MHz, DMSO- d_6) δ 14.38 (s, 2H), 12.87 (s, 2H), 7.20 (s, 2H), 6.74 (s, 2H), 6.33 (s, 2H), 2.05 (s, 6H), assignments referencing to the literature [36,37]; ^{13}C NMR (75 MHz, DMSO- d_6) δ (15 pairs of signals are overlapping) 184.4, 173.8, 168.3, 160.0, 142.5, 136.2, 129.7, 127.7, 125.8, 119.6, 118.7, 116.1, 113.3, 104.2, 21.3, assignments referencing to the literature [38]. MS (ESI) m/z : 505.2 (M-H) $^-$.

Synthesis of Hyp

Hyp (1.19 g, 60.4%) was synthesized following a literature protocol [35]. Data for Hyp: ^1H NMR (300 MHz, DMSO- d_6) δ 14.65 (s, 2H), 14.01 (s, 2H), 7.28 (s, 2H), 6.41 (s, 2H), 2.63 (s, 6H); ^{13}C NMR (75 MHz, DMSO- d_6) δ (15 pairs of signals are overlapping) 183.1, 174.3, 168.0, 161.1, 143.2, 126.7, 125.9, 121.1, 120.5, 119.2, 118.5, 108.3, 105.3, 101.8, 23.5, assignments referencing to the literature [38]. MS (ESI) m/z : 503.2 (M-H) $^-$.

Synthesis of ED-1 and ED-2

A solution of iron (III) chloride hydrate (1.95 g, 7.02 mmol) in ethanol (180 mL) was added drop wise to a solution of emodin anthrone (1.58 g, 5.85 mmol) in ethanol (375 mL) over 30 min. After heating for 4 h under reflux, the solution was poured into an aqueous solution of hydrochloric acid (5%, 750 mL). It was cooled to room temperature and the product

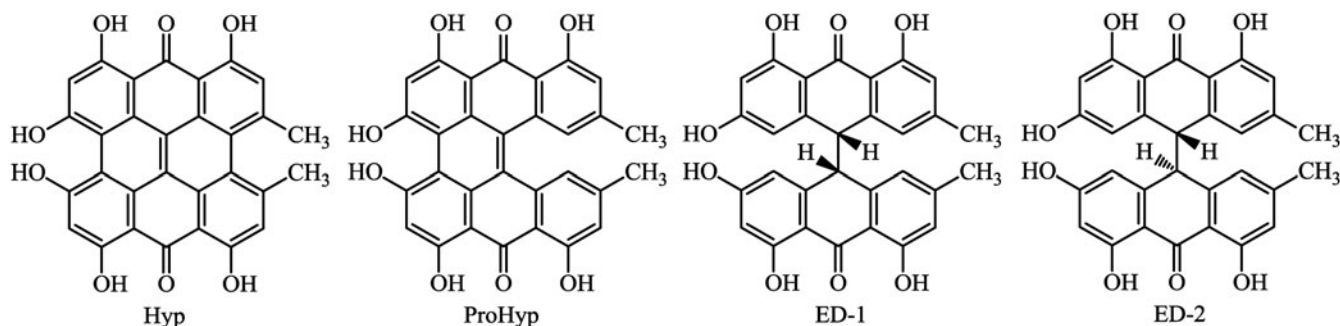


Figure 2. The chemical structures of the target compounds.

was extracted with ether. After drying over sodium sulfate and removal of the solvent, the residue was purified by column chromatography (chloroform:methanol = 50:1) to give emodin dianthrone 1.73 g, 58%) as a diastereomeric mixture. The diastereomeric mixture was further separated by preparative RP-HPLC (see Supplementary data) to yield ED-1 and ED-2. Data for ED-1; ^1H NMR (500 MHz, DMSO-d_6) δ 11.86 (s, 2H), 11.77 (s, 2H), 10.71 (s, 2H), 6.66 (s, 2H), 6.20 (s, 2H), 6.17 (d, $J = 1.5$ Hz, 2H), 6.02 (s, 2H), 4.45 (s, 2H), 2.22 (s, 6H), assignments referencing to the literature [36]; ^{13}C NMR (75 MHz, DMSO-d_6) δ 167.14, 138.32, 137.16, 137.01, 136.94, 136.79, 131.64, 130.97, 129.36, 129.22, 128.82, 128.39, 127.98, 127.69, 127.12, 123.32, 122.61, 115.81, 114.25, 110.16, 108.56, 102.68, 102.27, 52.56, 50.07. MS (ESI) m/z : 509.1 (M-H^-). Data for ED-2: ^1H NMR (500 MHz, DMSO-d_6) δ 11.92 (s, 2H), 11.68 (s, 2H), 10.79 (s, 2H), 6.61 (s, 2H), 6.22 (s, 2H), 6.22 (s, 2H), 6.00 (s, 2H), 4.43 (s, 2H), 2.17 (s, 6H), assignments referencing to the literature [36]; ^{13}C NMR (75 MHz, DMSO-d_6) δ 167.14, 138.32, 137.16, 137.01, 136.94, 136.79, 131.64, 130.97, 129.36, 129.22, 128.82, 128.39, 127.98, 127.69, 127.12, 123.32, 122.61, 115.81, 114.25, 110.16, 108.56, 102.68, 102.27, 52.56, 50.07. MS (ESI) m/z : 509.0 (M-H^-).

Radiolabeling and *in vitro* stability

The compounds were radiolabelled with ^{131}I via a direct oxidation reaction using iodogen as an oxidation agent. Briefly, iodogen (1, 3, 4, 6-tetrachloro-3 α , 6 α -diphenylglycouril; Pierce Biotechnology, ZI Camp Jouven, France) is first dissolved in dichloromethane and is coated on the wall of the Eppendorf tube according to the required dose (40–60 μg). To an iodogen-coated tube were added 400 μL of 0.5 mg/mL of each compound in DMSO and 100 μL of fresh Na^{131}I solution (37 MBq). The method of controlling variables (temperature, reaction time and the amount of iodogen) was used to optimize the radiolabeling yields. Radiochemical yield of each ^{131}I -dianthrone was determined using RP-HPLC (analysis methods are seen in the Supplementary data).

In vitro stabilities of ^{131}I -compounds were determined by incubation in rat serum at 37 $^\circ\text{C}$ for 72 h and monitored for degradation by RP-HPLC. Briefly, 100 μL of each reaction solution was added into 900 μL of rat serum and incubated at 37 $^\circ\text{C}$ for 72 h. After the incubation, 1 mL of a mixture of ethanol and acetonitrile (1:1, v/v) was added to precipitate the

serum proteins. The resulting mixture was centrifuged at 12 000 rpm for 10 min to collect the supernatant. The supernatant was filtered through 0.22- μm pore-size filters (Membrana, Germany) and then injected into RP-HPLC for analysis using the method described above.

Induction of cell necrosis

An *in vitro* model of necrosis was set up whereby A549 cells were treated with the H_2O_2 and analysed for FITC-annexin V and propidium iodide (PI) binding by flow cytometry. The human lung cancer A549 cell line was obtained from American Type Culture Collection (Manassas, VA). The A549 cells were seeded into a six-well cell culture plate at a density of 2.5×10^5 cells/well and incubated at 37 $^\circ\text{C}$ for 24 h. After being washed once with phosphate-buffered saline (PBS), cells were incubated at 37 $^\circ\text{C}$ for 1 h in the presence of increasing concentrations of H_2O_2 (0, 20, 40, 60, 80, 100, 120 mM) in 1 mL of RPMI-1640 medium. After incubation, the reaction medium was aspirated and the cells were rinsed once with 1 mL of cold pH 7.4 PBS to remove the remaining H_2O_2 . Necrosis and apoptosis were both assessed by using the annexin V/PI kit according to the manufacturer's instructions (Roche, France). Briefly, cells (5×10^5) were washed twice with PBS and suspended in annexin V and PI staining solution for 15 min at room temperature. Cells were analysed immediately on a flow cytometer (FACS Calibur; BD Biosciences, Franklin Lakes, NJ).

In vitro necrotic binding assay

The binding of ^{131}I -Hyp, ^{131}I -ProHyp, ^{131}I -ED-1 and ^{131}I -ED-2 for the cell were determined in A549 cells. The cell binding assay was replicated in triplicate for each ^{131}I -compound. Control group cells and 100 mM H_2O_2 treated cells were respectively transferred into 4 mL tubes and coincubated at 37 $^\circ\text{C}$ for 15 min with 0.037 MBq of ^{131}I -Hyp, ^{131}I -ProHyp, ^{131}I -ED-1 or ^{131}I -ED-2 in 1 mL of RPMI-1640 medium. After incubation at 37 $^\circ\text{C}$ for 15 min, the mixture was transferred into 1.5 mL tubes and centrifuged at 12 000 rpm for 10 min. The tubes were frozen in liquid nitrogen, the bottom tips containing the cell pellet were cut off, and the cell pellets and supernatants were collected and counted for radioactivity in a WIZARD² 2470 automated gamma counter (PerkinElmer, Maltham, MA). The data were expressed as activity ratios of the cell pellets to the cell pellets and supernatants ($[\text{cpm of cell pellets}/\text{cpm of cell pellets and supernatants}] \times 100\%$).

Animal models of necrosis

Adult male SD rats weighing 250–300 g were provided by Experimental Animal Center, Jiangsu Academy of Traditional Chinese Medicine (Nanjing, China). All animal studies were approved by the Institutional Animal Care and Use Committee.

Reperused partial liver infarction: Adult male SD rats were anaesthetized with intraperitoneal injection of pentobarbital (Nembutal Veterinary; Sanofi Sante Animale, Paris, France) at a dose of 40 mg/kg. Under laparotomy, reperused hepatic infarction was induced by temporarily clamping the hilum of the right liver lobes for 3 h. After reperfusion by declamping hepatic inflow and by giving massage to the liver lobe, the abdominal cavity was closed with two-layer sutures and the animals were allowed to recover overnight. Moreover, sham operated rats, which were subjected to the same surgery except for not clamping the hilum of the right liver lobes, were also established to be used for control in SPECT/CT imaging study.

Ethanol induced muscle necrosis: Each rat of reperused hepatic infarction was then intramuscularly injected with 0.2 mL absolute alcohol in the left hind limb to establish the model of chemically induced muscle necrosis. Thus, each rat model had both liver necrosis and muscle necrosis and was allowed to recover overnight after the procedure.

In vivo MRI examination

Magnetic resonance imaging (MRI) was performed to examine whether the model of liver necrosis and muscle necrosis were successfully established. Under anesthesia with 2% isoflurane in a mixture of 20% oxygen and 80% room air, the rat models placed in a wrist coil were scanned using a 1.5 T whole body MRI scanner (Echo speed; GE Co., New York, NY). MRI with T1-, T2- and DWI sequences was performed to acquire T1-weighted imaging (T1WI), T2-weighted imaging (T2WI) and diffusion-weighted imaging (DWI). Moreover, Dotarem (Gd-DOTA, Guerbet, France) was intravenously injected at a dose of 0.2 mmol/kg to obtain contrast enhanced-T1WI (CE-T1WI).

Drug delivery protocol

In order to facilitate intravenous (IV) administration, the solution after radioactive labeling reaction was diluted with polyethylene glycol 400 (PEG400) and propylene glycol (1:1, v/v) to formulate preparation immediately before injection. On day 1 after reperfusion of the partial liver infarction and induction of muscle necrosis, ^{131}I -Hyp, ^{131}I -ProHyp, ^{131}I -ED-1 or ^{131}I -ED-2 preparation was administered via the tail vein (14.8 MBq/kg according to ^{131}I dose and 0.2 mg/kg according to compound dose) under anaesthesia for biodistribution and pharmacokinetic studies. For biodistribution study, each rat model was intravenously injected with 0.1 mL of 1% Evans blue solution for intravital staining of necrosis at 8 h before being euthanized.

Biodistribution, autoradiography and histochemical staining

For each ^{131}I -compound, rat models with RPLI and muscle necrosis were randomly allocated into two groups of four

animals. After IV administration of ^{131}I -Hyp, ^{131}I -ProHyp, ^{131}I -ED-1 or ^{131}I -ED-2, the urine and feces were collected for gamma counting during the whole experiment and then the rats were sacrificed at 24 h and 72 h post injection (p.i.) ($n = 4$ per time point). Organs of interest were isolated, weighed and counted in a WIZARD² 2470 automated gamma counter (PerkinElmer, Waltham, MA). The stomach and intestines were emptied of food contents and the bladder was emptied of urine prior to radioactivity measurements. The necrotic liver and muscle tissues that were labeled by Evans blue were carefully sampled for gamma counting. Corrections were made for background radiation and physical decay during counting. Radioactive uptake in the organs was expressed as percentage of the injected dose per gram of tissues (%ID/g) while radioactive content in excretion was expressed as percentage of the injected dose (%ID).

After gamma counting, representative tissues of necrotic liver, normal liver and necrotic muscle were cryosectioned into 30 μm thick slices with a cryotome (Shandon Cryotome FSE; Thermo Fisher Scientific Co., Waltham, MA). Autoradiography were performed by exposing the sections to a high performance phosphor screen (PerkinElmer, Waltham, MA) for 4–48 h. Digital autoradiographic images were obtained by reading out the phosphor screen using a Cyclone Plus Phosphor Imager (PerkinElmer, Waltham, MA). Regions of interest (ROI) from the images were analyzed with OptiQuantTM software (version 5.0; Canberra-Packard, Meriden, CT). Ratios of radioactivity concentration (DLU/ mm^2) between ROIs on necrotic and viable areas were calculated. Afterwards, the sections were stained with hematoxylin and eosin (H&E) using the conventional procedure and were digitally photographed for macroscopic inspection.

Pharmacokinetics study

Another six rat models with RPLI and muscle necrosis was used for pharmacokinetics study. After IV administration of ^{131}I -Hyp, ^{131}I -ProHyp, ^{131}I -ED-1 or ^{131}I -ED-2, 10 μL of blood samples were collected via a tail incision at 5 min, 10 min, 30 min, 1 h, 2 h, 3 h, 4 h, 6 h, 8 h, 12 h, 24 h and 48 h p.i. Blood samples were measured for radioactive counts in a WIZARD² 2470 automated gamma counter (PerkinElmer, Waltham, MA) and corrections were made for its background radiation and physical decay during counting. Radioactivity concentrations in blood samples were calculated and expressed as megabecquerel per liter (MBq/L). The pharmacokinetic parameters including area under the curve ($\text{AUC}_{(0-t)}$, $\text{AUC}_{(0-\infty)}$), elimination half-life ($t_{1/2z}$), peak time (T_{max}), clearance (CL_z), peak concentration (C_{max}) and apparent volume of distribution (V_z) were calculated by Drug and Statistics for windows 2.0 software.

SPECT/CT imaging

^{131}I -Hyp was evaluated for its ability to image necrosis *in vivo* in rats with RPLI or sham surgery. Approximately, 14.8 MBq/kg of ^{131}I -Hyp was injected into rats with RPLI or sham surgery via the tail vein. SPECT/CT imaging was performed using a variable-angle dual-detector SPECT with 6-slice CT (Symbia T6; Siemens Medical Systems Inc., Chicago, IL). Rats were anaesthetized by intraperitoneal injection of

sodium pentobarbital at a dose of 30 mg/kg and then secured to the head holder of the patient bed in supine position. SPECT/CT images were acquired at 24 h and 72 h after intravenous injection of ^{131}I -Hyp using the following acquisition parameters: static image matrix size 128×128 , acquisition count limit 50000, SPECT tomographic image matrix 64×64 , and continuous acquisition 15 s/frame \times 24 frames.

Statistical analysis

Numerical data were expressed as mean \pm standard deviation (SD), unless otherwise stated. Statistical significance in all experiments was determined by unpaired two-tailed Student's *t* test, $p < 0.05$ was considered significant.

Results

Synthesis

All the target compounds were successfully synthesized starting with the coupling of two molecules of emodin anthrone. The desired intermediate emodin anthrone was prepared from commercially available emodin in high yields. Emodin dianthrone was synthesized as a diastereomeric mixture in the presence of iron (III) chloride hydrate in anhydrous ethanol. The diastereomers are inseparable in silica gel TLC plate and slightly separable in reversed phase TLC plate. They were successfully separated into ED-1 and ED-2 by preparative RP-HPLC.

Radiolabeling and *in vitro* stability

The radiolabeling method [39] used for radioiodination of the target compounds was simple and effective in this work. All target compounds were readily radiolabeled with ^{131}I with greater than 95% radiolabeling yields. The retention times of ^{131}I -Hyp, ^{131}I -ProHyp, ^{131}I -ED-1 and ^{131}I -ED-2 were 14.40, 13.52, 12.03 and 12.66 min, respectively. Stabilities of all four ^{131}I -dianthrone were favorable in rat serum at 37 °C for 72 h (Figure 3).

Induction of cell necrosis

Necrosis was induced by H_2O_2 with concentrations of 20, 40, 60, 80, 100, 120 mM for 1 h. As shown in Figure 4(A), the percentage of necrotic cells as evaluated by flow cytometry increased with the concentration of H_2O_2 from 20 mM to 100 mM while slightly declined with 120 mM. Untreated A549 cells (control cells) showed 4.71% of necrotic cells, whereas cells treated with increasing H_2O_2 concentrations for 1 h showed gradually increasing necrotic cells from 20.84% to a maximum of 78.13% of necrotic cells with 100 mM H_2O_2 (Figure 4). The percentage of apoptotic cells reached a maximum of 13.60% with 20 mM H_2O_2 but there was no proportional change with H_2O_2 concentration. It is worth noting that there is no significant difference on the percentage of apoptotic cells between controls and treated with 100 mM H_2O_2 cells (6.22% versus 6.64%, $p > 0.5$).

In vitro necrotic binding assay

In order to determine the effect of structure on necrosis targeting of ^{131}I -dianthrone, *in vitro* binding studies with

H_2O_2 treated A549 cells were performed. All four tracers were found to have a significantly higher uptake for 100 mM H_2O_2 treated cells compared to non-treated cells (Figure 5). The ratio of percentage of radioactivity in the pellet for the treated cells compared with non-treated cells were 8.10 for ^{131}I -Hyp, 5.27 for ^{131}I -ProHyp, 3.08 for ^{131}I -ED-1 and 2.22 for ^{131}I -ED-2. These results demonstrated that the skeleton structure had a profound influence on necrosis targeting ability for the four radiotracers.

In vivo MRI examination

All rats survived the anesthesia and surgical procedures. Model rats with RPLI and absolute ethanol induced muscular necrosis were successfully established as proven by MRI. The necrotic liver lobe showed homogeneously isointense on T1WI but hyperintense relative to the adjacent normal liver on T2WI, DWI and contrast enhanced T1WI. The necrotic area in the left leg showed iso- or slightly hyperintense on T1WI but hyperintense on T2WI, DWI and contrast enhanced T1WI compared with the healthy right leg (Figure 6).

Biodistribution and excretion

The biodistribution properties of ^{131}I -Hyp, ^{131}I -ProHyp, ^{131}I -ED-1 and ^{131}I -ED-2 are illustrated in Figure 7 with the results expressed as mean %ID/g \pm SD. The excretion results are depicted in Figure 8, where the radioactivity of urine and feces are expressed as mean %ID \pm SD. Among these four ^{131}I -dianthrone, ^{131}I -Hyp showed the highest necrotic liver and necrotic muscle uptake both at 24 h and 72 h p.i. Despite higher radioactivity uptake in most normal tissues, ^{131}I -Hyp had lowest radioactivity retention in normal liver, which results in the highest necrotic to normal liver ratio. Although it had higher radioactivity uptake in normal muscle, ^{131}I -Hyp still exhibited the highest necrotic/normal muscle ratio. The higher radioactivity uptake and slow clearance in the lung demonstrated that ^{131}I -Hyp may form coarse aggregates in the physiological environment and were subsequently trapped by pulmonary capillary network. ^{131}I -ProHyp exhibited similar necrosis uptake pattern to ^{131}I -Hyp. Although it showed much lower radioactivity uptake and rapid clearance in the lung, ^{131}I -ProHyp also exhibited much lower radioactivity uptake in necrotic liver and muscle in comparison with ^{131}I -Hyp. ^{131}I -ED-1 and ^{131}I -ED-2 exhibited similar radioactivity uptake pattern in both normal and necrotic tissues. Among these studied ^{131}I -dianthrone, ^{131}I -ED-1 and ^{131}I -ED-2 presented the lowest radioactivity uptake in necrotic tissues and had the lowest necrotic/normal tissue ratio.

As described in Figure 8, ^{131}I -Hyp was mainly cleared through the hepatobiliary pathway resulting in increasing feces radioactivity with time. More than 61.0%ID of ^{131}I -Hyp was excreted via feces and only 11.1%ID of ^{131}I -Hyp were excreted via urine at 72 h p.i. ^{131}I -ProHyp was also mainly cleared via the hepatobiliary pathway and to a lesser extent via the renal pathway, resulting in 31.3%ID of ^{131}I -ProHyp in feces and 26.4%ID of ^{131}I -ProHyp in urine within 72 h. Unlike ^{131}I -Hyp and ^{131}I -ProHyp, excretion of ^{131}I -ED-1 and ^{131}I -ED-2 was mainly via the renal pathway and to a lesser extent via the hepatobiliary pathway.

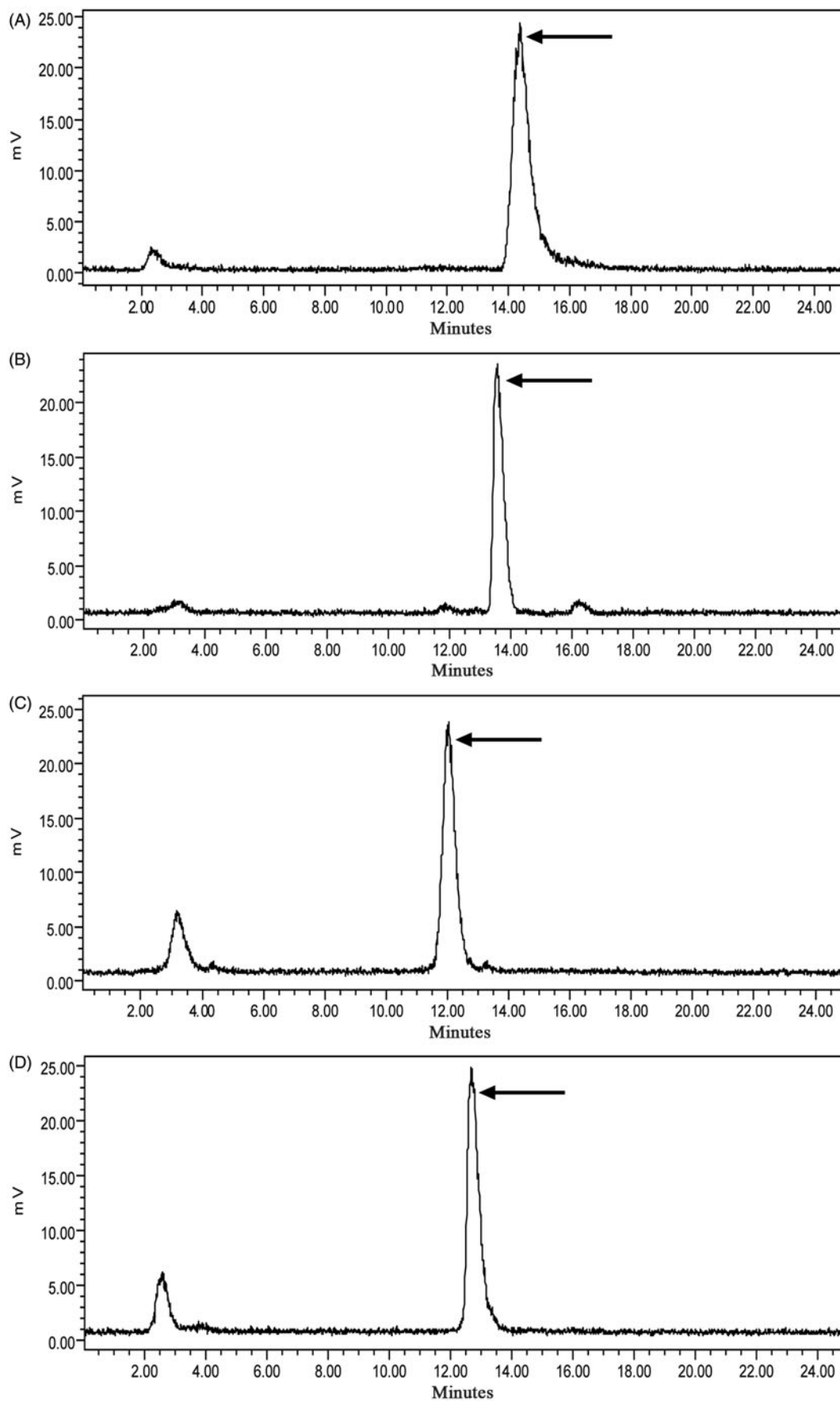


Figure 3. Radioactive HPLC profiles of ^{131}I -Hyp (A), ^{131}I -ProHyp (B), ^{131}I -ED-1 (C) and ^{131}I -ED-2 (D) in rat serum after incubation at 37 °C for 72 h. The arrows denote the peaks corresponding to intact ^{131}I -Hyp (14.40 min), ^{131}I -ProHyp (13.52 min), ^{131}I -ED-1 (12.03 min) and ^{131}I -ED-2 (12.66 min).

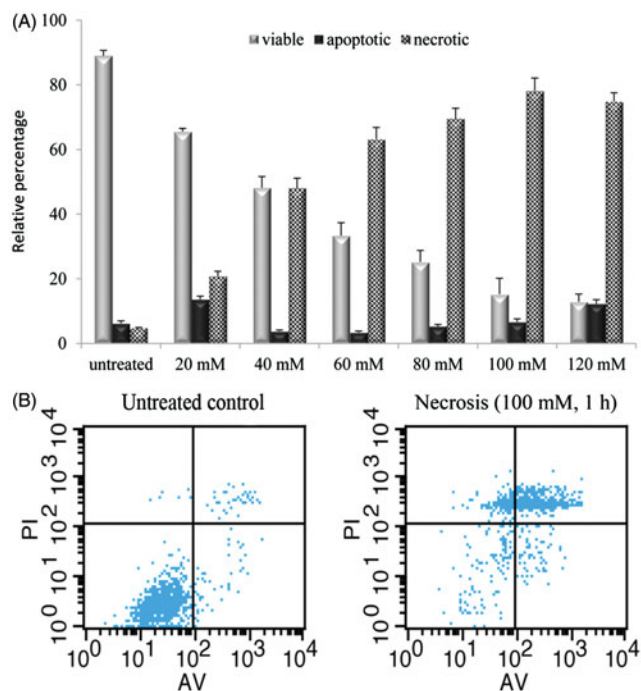


Figure 4. (A) *In vitro* determination of the percentage of viable, apoptotic and necrotic cells by flow cytometry after the treatment of A549 cells with increasing concentrations of H₂O₂. The results are expressed as the percentage relative to the mean of fluorescence, mean \pm SD, $n = 3$. (B) Cytograms obtained with untreated A549 cells and those treated with 100 mM H₂O₂ for 1 h. Apoptotic cells (annexin-V-positive, PI-negative) were on the lower right gate, necrotic cells (annexin-V-positive or -negative, PI-positive) were on the upper right and left gate and viable cells (annexin-V-negative, PI-negative) were on the lower left gate.

Postmortem autoradiography and histochemical staining

The representative autoradiographs and corresponding H&E staining images of the liver (Figure 9A) and muscle slices (Figure 9B) at 24 h and 72 h p.i. for each ¹³¹I-dianthrone are shown in Figure 9. Hepatic infarct and muscle necrosis was identified by H&E staining. Autoradiography showed that radioactivity uptake in necrotic liver was much higher than that in normal liver for each ¹³¹I-dianthrone, particularly for ¹³¹I-Hyp. Moreover, necrosis targetability of ¹³¹I-dianthrone was further verified in muscle tissue as higher radioactivity uptake was seen in the necrotic areas than that in the viable areas. By a semiquantitative analysis, ratios of radioactivity in necrotic over normal tissues obtained from the representative autoradiographs are presented in Table 1. At 24 h and 72 h p.i., the necrotic to normal liver uptake ratios for ¹³¹I-Hyp were 20.9 and 46.4, respectively; for necrotic to normal muscle, these values were 9.0 and 13.8.

Pharmacokinetics

The mean plasma radioactive concentration–time profiles of ¹³¹I-dianthrone from 0 to 48 h in rat models with RPLI and muscle necrosis are shown in Figure 10. The major pharmacokinetic parameters are presented in Table 2. Although there was no significant difference in $t_{1/2z}$ for ¹³¹I-Hyp and ¹³¹I-ProHyp ($p > 0.05$), the C_{max} value for ¹³¹I-Hyp

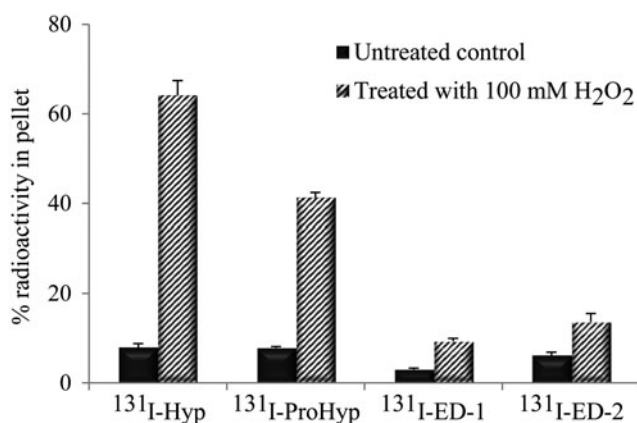


Figure 5. Histogram representation of *in vitro* binding experiment. The percentage of radioactivity in the pellet is shown for ¹³¹I-Hyp, ¹³¹I-ProHyp, ¹³¹I-ED and ¹³¹I-ED in non-treated (control) and H₂O₂-treated A549 cells. For all four tracers, the percentage of radioactivity in the pellet is significantly increased for the treated cells in comparison to control cells.

was significantly higher than that for ¹³¹I-ProHyp ($p < 0.01$) and the same is true for the $AUC_{(0-t)}$ ($p < 0.01$) and $AUC_{(0-\infty)}$ ($p < 0.01$). The blood clearance of ¹³¹I-ED-2 was similar to that of ¹³¹I-ED-1, as the $t_{1/2z}$, CL_z and V_z with no statistically significant difference ($p > 0.05$). Although the C_{max} value for ¹³¹I-ED-2 was significantly higher than that for ¹³¹I-ED-1 ($p < 0.01$), both $AUC_{(0-t)}$ ($p > 0.05$) and $AUC_{(0-\infty)}$ ($p > 0.05$) were similar to each other.

SPECT/CT imaging

As ¹³¹I-Hyp showed higher necrotic liver uptake and lower normal liver uptake than the other three ¹³¹I-dianthrone at 24 h and 72 h p.i., we further evaluated its ability for imaging necrosis *in vivo* in rats with RPLI or sham surgery. Representative SPECT/CT images at 24 h and 72 h p.i. of ¹³¹I-Hyp are presented in Figure 11. On the SPECT/CT images, the uptake of radioactivity in the infarcted liver lobe was apparently much higher than that in the non-infarcted liver lobe and that in the liver of the sham-operated rat. Right infarcted liver lobes could be clearly visualized by SPECT/CT using ¹³¹I-Hyp as an imaging probe, which suggested that specific high uptake of ¹³¹I-Hyp in the infarcted liver was mediated by necrosis and ¹³¹I-Hyp can detect necrosis in the liver after a partial liver infarction. The SPECT/CT images of rats with RPLI showed high contrast of infarcted liver lobes to normal liver lobes, which was consistent with the biodistribution results. Moreover, higher radioactivity uptake was seen especially in the intestines, indicating the major excretion pathways of the compound.

Discussion

In our previous reports [33,40,41], we have perceived the important effect of skeleton structure of dianthrone on their necrosis targeting. In order to ascertain in more detail the relationship between molecular skeleton structures of dianthrone and their necrosis targeting and clearance properties, we synthesized and evaluated ¹³¹I-Hyp, ¹³¹I-ProHyp, ¹³¹I-ED-1 and ¹³¹I-ED-2 in *in vitro* cell of induced necrosis and in *in vivo* model rats of induced necrosis.

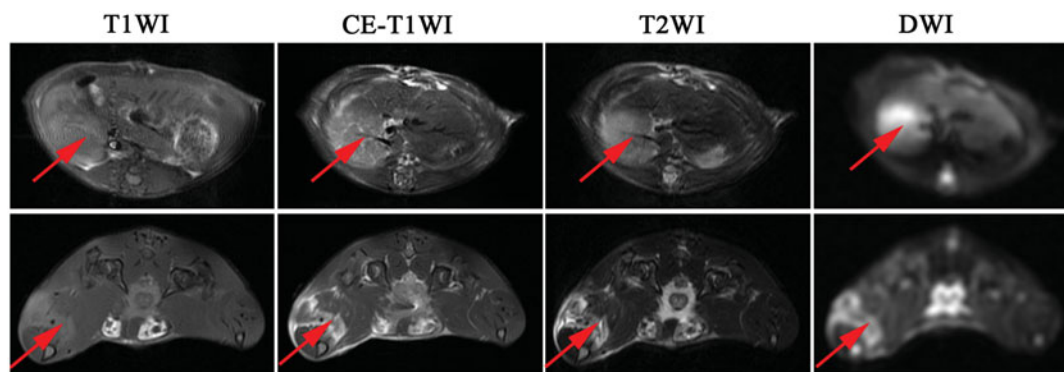


Figure 6. *In vivo* MRI transverse section images of rat model with RPLI and muscle necrosis. The upper row was T1WI, CE-T1WI, T2WI and DWI of the liver with infarcted right lobe (arrow) and the bottom row was that of the leg with muscle necrosis (arrow). Infarcted liver lobe and necrotic muscle appeared hyperintense on CE-T1WI, T2WI and DWI.

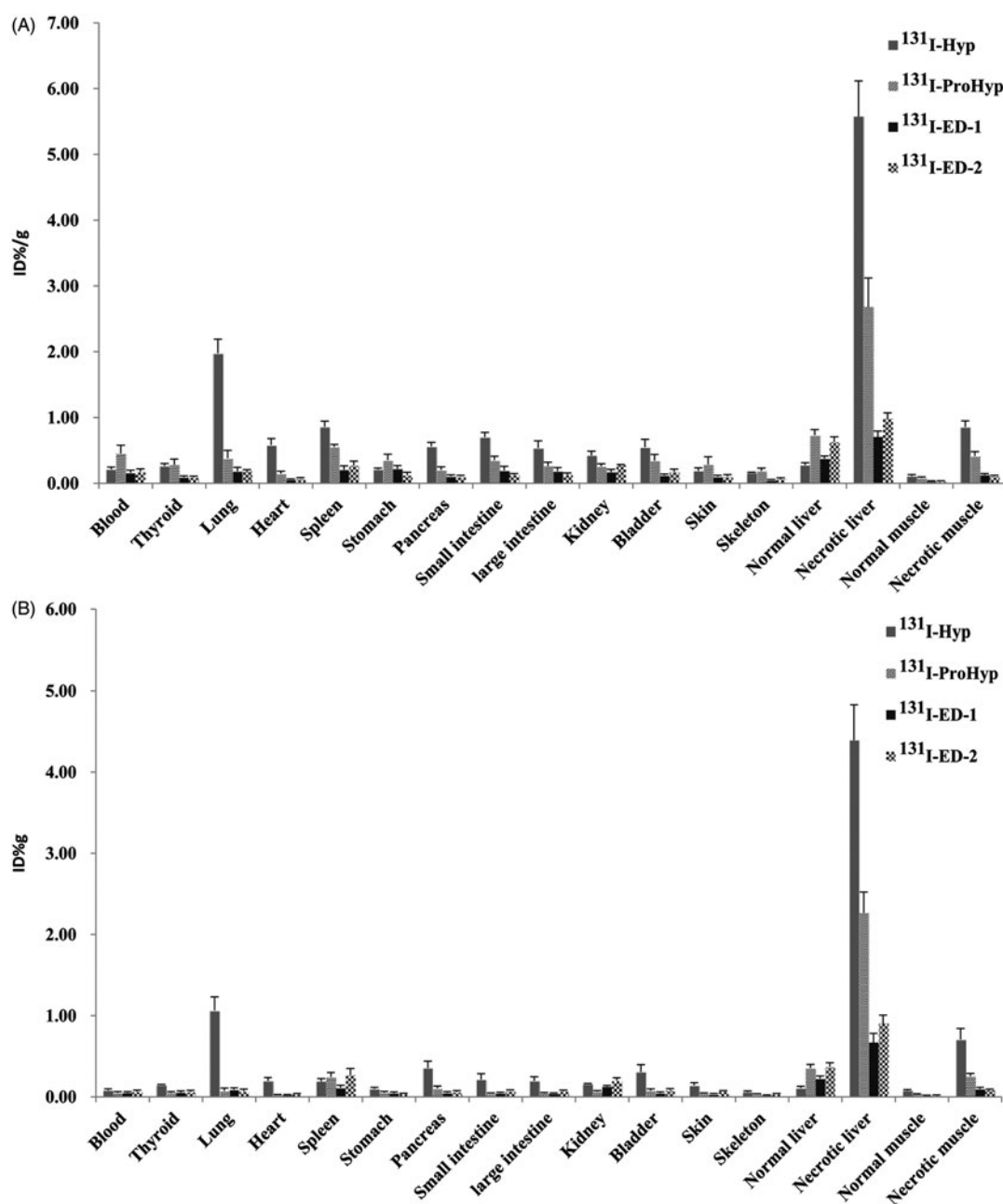


Figure 7. Biodistribution of ^{131}I -dianthrones in rat models with RPLI and muscle necrosis at 24 h (A) and 72 h (B) p.i. ($n = 4$ per time point).

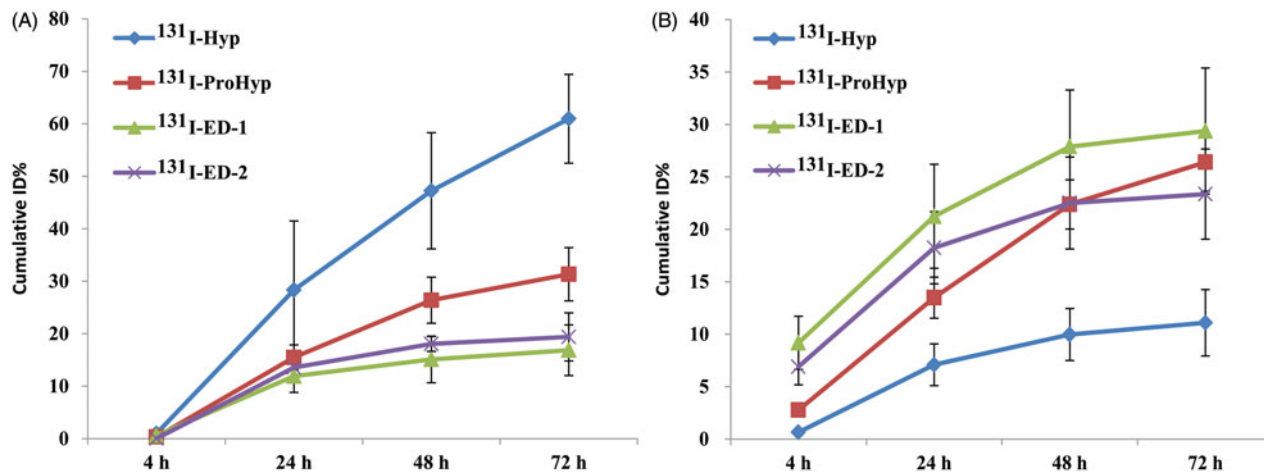


Figure 8. Excretion of ^{131}I -dianthrones by the feces (A) and urine (B) in rat models of induced necrosis within 72 h p.i. ($n \geq 4$ per time point).

Figure 9. Representative autoradiographs (upper row for each ^{131}I -dianthrones) and corresponding H&E images (lower row for each ^{131}I -dianthrones) of liver slices (A) and muscle slices (B) from the rat models at 24 h and 72 h p.i., respectively. The left column represents the normal liver and the right column represents the necrotic liver at each time point in A. Each muscle section contains both normal muscle and necrotic muscle in B. N = necrotic area, V = viable area.

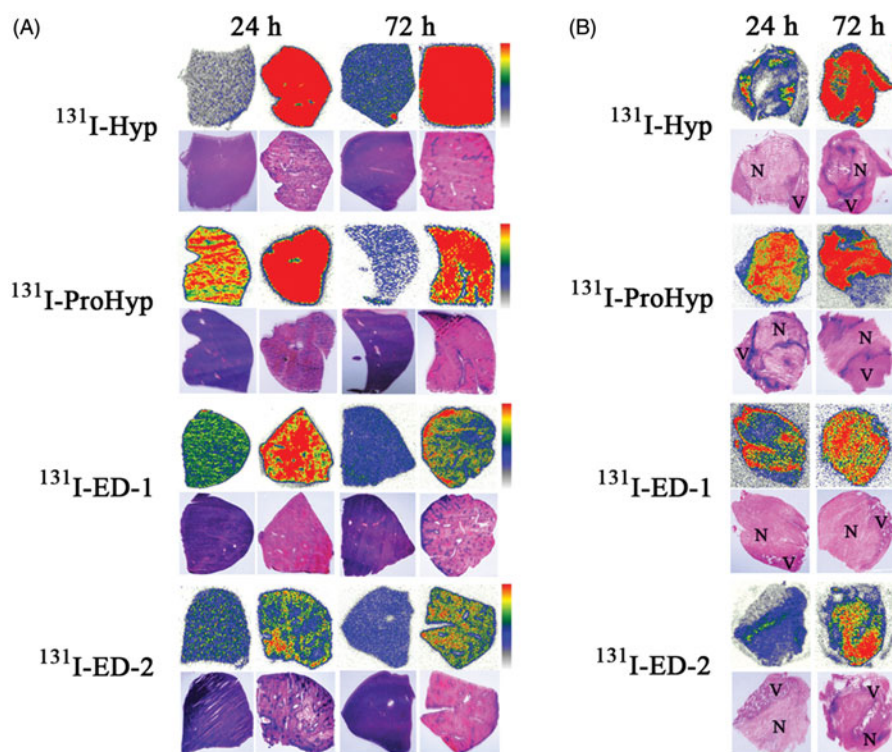


Table 1. Ratios of radioactivity uptake between ROIs on necrotic and viable areas from rat models with RPLI and muscle necrosis at 24 h and 72 h after IV injection of ^{131}I -dianthrones*.

Compounds	Necrotic liver/ normal liver		Necrotic muscle/ normal muscle	
	24 h	72 h	24 h	72 h
^{131}I -Hyp	20.9	46.4	9.0	13.8
^{131}I -ProHyp	4.3	7.9	6.3	9.1
^{131}I -ED-1	2.8	4.1	5.0	7.5
^{131}I -ED-2	2.4	3.2	4.5	5.4

*Regions of interest (ROI) from the autoradiographic images was analyzed with Optiquant software. Radioactivity uptake on ROIs on necrotic and viable areas was expressed as DLU/mm². Ratios were calculated by dividing DLU/mm² of ROI on necrotic areas by that on viable areas.

The present study showed that the disruption of molecular planarity has a dramatic impact on the necrosis targeting of the ^{131}I -dianthrones. With the increasing distortion of molecular planarity, the necrosis targeting also continues to reduce. Among the four ^{131}I -dianthrones, ^{131}I -Hyp displayed the highest percentage of radioactivity in the pellet for the treated cells followed by ^{131}I -ProHyp, whereas ^{131}I -ED-1 and ^{131}I -ED-2 exhibited significantly lower percentage of radioactivity in the pellet for the treated cells. *In vivo* biodistribution study displayed a similar necrotic tissue uptake pattern. Up to now, the mechanism of necrosis avidity behind Hyp and other NAAs has not yet been fully elucidated, although several thoughts or hypotheses were raised to explain the phenomenon, such as cholesterol or phospholipid binding in lipid membranes, or a compound-specific mechanism behind

Figure 10. The mean plasma radioactive concentration–time profiles following a single IV administration of ^{131}I -dianthrones in rat models with RPLI and muscle necrosis. Data are expressed as mean \pm SD ($n = 6$, each group).

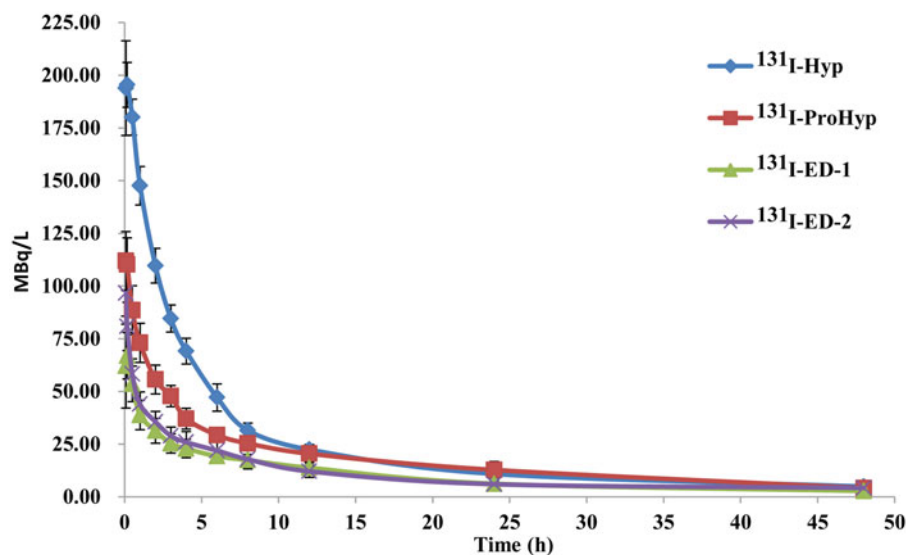
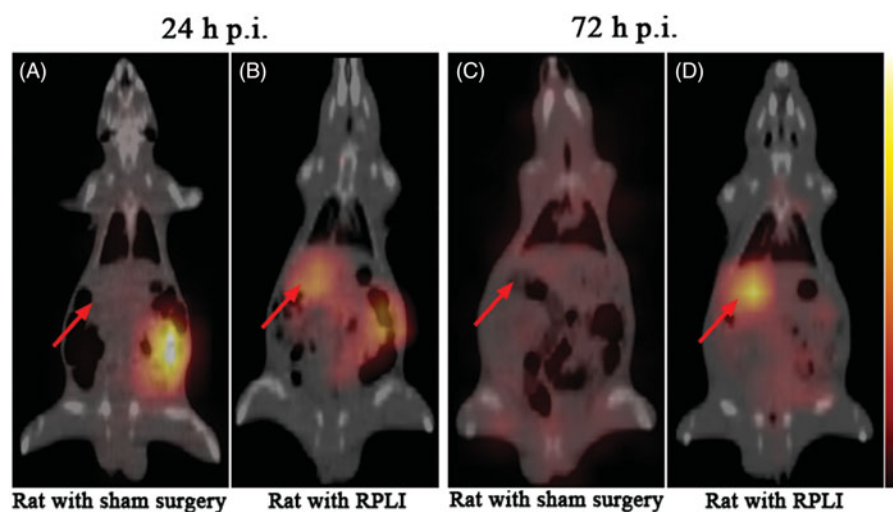


Table 2. Major pharmacokinetic parameters of ^{131}I -dianthrones obtained by non-compartmental modeling after IV injection in rat models with RPLI and muscle necrosis within 48h ($n = 6$).

Parameters	Unit	Major pharmacokinetic parameter value for ^{131}I -dianthrones			
		^{131}I -Hyp	^{131}I -ProHyp	^{131}I -ED-1	^{131}I -ED-2
$\text{AUC}_{(0-t)}$	MBq/L*h	1178.41 \pm 62.92	864.80 \pm 129.92	509.71 \pm 71.50	540.82 \pm 104.35
$\text{AUC}_{(0-\infty)}$	MBq/L*h	1268.36 \pm 48.63	955.14 \pm 151.52	546.83 \pm 79.04	557.92 \pm 108.16
$t_{1/2z}$	h	14.73 \pm 2.77	15.05 \pm 1.28	12.71 \pm 2.70	10.05 \pm 1.25
T_{max}	h	0.15 \pm 0.04	0.13 \pm 0.05	0.14 \pm 0.04	0.08 \pm 0
CL_z	L/h/kg	0.01 \pm 0	0.02 \pm 0	0.03 \pm 0	0.03 \pm 0.01
C_{max}	MBq/L	200.57 \pm 18.38	114.86 \pm 11.84	68.73 \pm 12.81	96.56 \pm 10.84
V_z	L/kg	0.25 \pm 0.05	0.34 \pm 0.05	0.50 \pm 0.12	0.40 \pm 0.09

The values are expressed as mean \pm SD.

Figure 11. ^{131}I -Hyp can image tissue necrosis *in vivo* after a partial liver infarction. (A) and (C) Representative SPECT/CT images of rat with sham surgery at 24 h and 72 h post injection of ^{131}I -Hyp, respectively. (B) and (D) Representative SPECT/CT images of rat with RPLI at 24 h and 72 h post injection of ^{131}I -Hyp, respectively.



the necrosis targeting of different NAAs [22]. Although we have demonstrated that the Hyp compounds are indeed more effective than the ED compounds both *in vitro* and *in vivo*, we don't know the exact cause yet. As we know, Hyp has a nearly planar rigid skeleton. The skeleton structure of ProHyp is less planar than that of Hyp as a result of the

absence of a single bond. Emodin dianthrones can be free to rotate around a single bond connecting two molecules of emodin anthrone and the overall rigidity was completely broken. Therefore, by analyzing structure–necrosis targeting relationship of the four dianthronone compounds, we can at least draw the conclusion that rigid skeleton structure may play an

important role in necrosis targeting and molecular morphology of a rigid nearly planar configuration may be more beneficial to its binding to the target site.

The difference in pharmacokinetic behavior suggested that skeleton structures of ^{131}I -dianthrones have also a profound influence on their pharmacokinetic properties. Fonge et al. [42] confirmed that ^{131}I -Hyp bind mainly to low-density lipoprotein (LDL) and to a lesser extent to high-density lipoprotein (HDL), which was similar to plasma protein binding profile of Hyp. Considering the similarity in structure that both ^{131}I -Hyp and ^{131}I -ProHyp maintain a nearly planar structure, we have reason to believe that ^{131}I -ProHyp could have a similar plasma lipoprotein binding profile to ^{131}I -Hyp. This may explain why they showed similar $t_{1/2z}$ ($p > 0.05$) despite the fact that lipophilicity of ^{131}I -ProHyp ($\log P = 2.40 \pm 0.18$) [42] is less than that of ^{131}I -Hyp ($\log P = 3.08 \pm 0.03$) [43]. This indicates that not only lipophilicity but also other parameters have a significant impact on the pharmacokinetic properties of the ^{131}I -dianthrones. Furthermore, the C_{\max} value for ^{131}I -Hyp was nearly two times higher than that for ^{131}I -ProHyp, which may ensure sufficient hypericin that could be delivered to the target tissues. Although ^{131}I -ED-1 and ^{131}I -ED-2 displayed similar plasma radioactive concentration–time profiles, the higher C_{\max} ($p < 0.01$) for ^{131}I -ED-2 relative to ^{131}I -ED-1 suggested stereoisomerism have an influence on the pharmacokinetic parameters. Moreover, both the $\text{AUC}_{(0-t)}$ ($p > 0.05$) and $\text{AUC}_{(0-\infty)}$ ($p > 0.05$) values were not significantly different, which suggested they may have similar bioavailability after IV injection.

The results of present study showed that the skeleton structure of Hyp was the most attractive for the development of promising NAAs both for necrosis imaging and targeted radionuclide therapy. Further SAR study will involve the effect of various substituent groups on necrosis targeting of Hyp. Owing to the hydrophobic effect of its nearly planar highly conjugated structure and the cofacial π – π stacking between the molecular skeletons, Hyp is prone to form aggregates in an aqueous environment [30,44]. After intravenous administration, parts of the Hyp might form the aggregates and even coarse pellets in the blood circulation. The formed coarse aggregates are intercepted by mononuclear phagocyte system, especially by pulmonary capillary network, which not only reduces its biodistribution to necrotic tissues but also shows unwanted biodistribution in normal tissues [31,32]. Although distortion and even destruction of π -conjugated system may reduce the degree of self-aggregation of dianthrones, it also reduced their necrosis targeting. Accordingly, it is desirable to reduce the self-aggregation degree of Hyp without reducing the necrosis targeting as far as possible. A possible strategy is to introduce bulky groups to its rigid skeleton structure to improve the water solubility and hinder the cofacial π – π stacking [45,46].

The future development and application of Hyp necessitate a more complete knowledge of the necrosis-avidity mechanism. Not identifying the specific binding moiety that is responsible for the necrosis avidity of Hyp has seriously hindered our research process. Studies have indicated that Hyp can bind to DNA molecule and 5'AG3' doublet is a specific DNA target for Hyp binding *in vitro* [47]. Therefore,

the next step, we attempt to study whether DNA binding is responsible for high Hyp targeting to necrosis region.

Conclusions

The present study demonstrated that the destruction of rigid skeleton structure dramatically reduced the necrosis targeting ability of ^{131}I -dianthrones. ^{131}I -Hyp exhibited sustaining higher necrosis tissue uptake and lower normal liver uptake than those of the other three ^{131}I -dianthrones. Hepatic infarction could be clearly visualized by SPECT/CT using ^{131}I -Hyp as an imaging probe. The preliminary SAR study indicated that the skeleton structure of Hyp was the most attractive for further developing NAAs. Future work will focus on reducing the self-aggregation degree of Hyp and understanding the mechanism that yields necrosis targeting in molecular level.

Acknowledgements

We thank Mr Changwen Fu and Mr Yu Fu, Department of Nuclear Medicine, the First Affiliated Hospital of Nanjing Medical University, for their wonderful work in SPECT/CT scanning.

Declaration of interest

The authors report no declaration of interest. This work was financially supported by the National Natural Science Foundation of China (81473120 and 21171092), the fourth phase of 333 projects in Jiangsu Province (BRA2012211), the Project Program of State Key Laboratory of Natural Medicines, China Pharmaceutical University (ZJ11175) and the Ninth Batch of ‘‘Six Talent Peaks’’ Project of Jiangsu Province (2012-YY-008).

References

1. Dasari M, Lee S, Sy J, et al. Hoechst-IR: an imaging agent that detects necrotic tissue *in vivo* by binding extracellular DNA. *Org Lett* 2010;12:3300–3.
2. Walker N, Harmon B, Gobe G, Kerr J. Patterns of cell death. *Methods Achiev Exp Pathol* 1987;13:18–54.
3. De Saint-Hubert M, Prinsen K, Mortelmans L, et al. Molecular imaging of cell death. *Methods* 2009;48:178–87.
4. Majno G, Joris I. Apoptosis, oncosis, and necrosis. An overview of cell death. *Am J Pathol* 1995;146:3–15.
5. Proskuryakov SY, Konoplyannikov AG, Gabai VL. Necrosis: a specific form of programmed cell death? *Exp Cell Res* 2003;283:1–16.
6. McConkey DJ. Biochemical determinants of apoptosis and necrosis. *Toxicol Lett* 1998;99:157–68.
7. Smith BA, Smith BD. Biomarkers and molecular probes for cell death imaging and targeted therapeutics. *Bioconjug Chem* 2012;23:1989–2006.
8. Van de Putte M, Marysael T, Fonge H, et al. Radiolabeled iodohypericin as tumor necrosis avid tracer: diagnostic and therapeutic potential. *Int J Cancer* 2012;131:E129–37.
9. Marysael T, Bauwens M, Ni Y, et al. Pretargeting of necrotic tumors with biotinylated hypericin using ^{125}I -labeled avidin: evaluation of a two-step strategy. *Invest New Drugs* 2012;30:2132–40.
10. Li J, Cona MM, Chen F, et al. Exploring theranostic potentials of radioiodinated hypericin in rodent necrosis models. *Theranostics* 2012;2:1010–19.
11. Li J, Cona MM, Chen F, et al. Sequential systemic administrations of combretastatin A4 phosphate and radioiodinated hypericin exert

- synergistic targeted theranostic effects with prolonged survival on SCID mice carrying bifocal tumor xenografts. *Theranostics* 2012;3:127–37.
12. Ji Y, Jiang C, Zhang X, et al. Necrosis targeted combinational theragnostic approach using radioiodinated sennidin A in rodent tumor models. *Oncotarget* 2014;5:2934–46.
 13. Bonte F, Parkey R, Graham K, et al. A new method for radionuclide imaging of myocardial infarcts I. *Radiology* 1974;110:473–4.
 14. Okada DR, Johnson G, Liu Z, et al. Early detection of infarct in reperfused canine myocardium using ^{99m}Tc -glucarate. *J Nucl Med* 2004;45:655–64.
 15. Liu Z, Barrett HH, Stevenson GD, et al. High-resolution imaging with ^{99m}Tc -glucarate for assessing myocardial injury in rat heart models exposed to different durations of ischemia with reperfusion. *J Nucl Med* 2004;45:1251–9.
 16. Orlandi C, Crane PD, Edwards DS, et al. Early scintigraphic detection of experimental myocardial infarction in dogs with technetium-99m-glucaric acid. *J Nucl Med* 1991;32:263–8.
 17. Khaw B, Gold HK, Yasuda T, et al. Scintigraphic quantification of myocardial necrosis in patients after intravenous injection of myosin-specific antibody. *Circulation* 1986;74:501–8.
 18. Khaw BA, Yasuda T, Gold HK, et al. Acute myocardial infarct imaging with indium-111-labeled monoclonal antimyosin Fab. *J Nucl Med* 1987;28:1671–8.
 19. Fonge H, Jin L, Wang H, et al. Synthesis and preliminary evaluation of mono- ^{123}I iodohypericin monocarboxylic acid as a necrosis avid imaging agent. *Bioorg Med Chem Lett* 2007;17:4001–5.
 20. Fonge H, Chitneni SK, Lixin J, et al. Necrosis avidity of $^{99m}\text{Tc}(\text{CO})_3$ -labeled pamoic acid derivatives: synthesis and preliminary biological evaluation in animal models of necrosis. *Bioconjugate Chem* 2007;18:1924–34.
 21. Cona MM, de Witte P, Verbruggen A, Ni Y. An overview of translational (radio)pharmaceutical research related to certain oncological and non-oncological applications. *World J Methodol* 2013;3:45–64.
 22. Jiang B, Wang J, Ni Y, Chen F. Necrosis avidity: a newly discovered feature of hypericin and its preclinical applications in necrosis imaging. *Theranostics* 2013;3:667–76.
 23. Song S, Xiong C, Zhou M, et al. Small-animal PET of tumor damage induced by photothermal ablation with ^{64}Cu -bis-DOTA-hypericin. *J Nucl Med* 2011;52:792–9.
 24. Ni Y, Huyghe D, Verbeke K, et al. First preclinical evaluation of mono- ^{123}I iodohypericin as a necrosis-avid tracer agent. *Eur J Nucl Med Mol Imaging* 2006;33:595–601.
 25. Fonge H, Vunckx K, Wang H, et al. Non-invasive detection and quantification of acute myocardial infarction in rabbits using MONO- ^{123}I iodohypericin microSPECT. *Eur Heart J* 2008;29:260–9.
 26. Cona MM, Feng Y, Li Y, et al. Comparative study of iodine-123-labeled hypericin and ^{99m}Tc -labeled hexakis [2-methoxy isobutyl isonitrile] in a rabbit model of myocardial infarction. *J Cardiovasc Pharmacol* 2013;62:304–11.
 27. Feng Y, Cona MM, Vunckx K, et al. Detection and quantification of acute reperfused myocardial infarction in rabbits using DISA-SPECT/CT and 3.0T cardiac MRI. *Int J Cardiol* 2013;168:4191–8.
 28. Van de Putte M, Wang H, Chen F, et al. Hypericin as a marker for determination of tissue viability after intratumoral ethanol injection in a murine liver tumor model. *Acad Radiol* 2008;15:107–13.
 29. Van de Putte M, Wang H, Chen F, et al. Hypericin as a marker for determination of tissue viability after radiofrequency ablation in a murine liver tumor model. *Oncol Rep* 2008;19:927–32.
 30. Bánó G, Staničová J, Jancura D, et al. On the diffusion of hypericin in dimethylsulfoxide/water mixtures – the effect of aggregation. *J Phys Chem B* 2011;115:2417–23.
 31. Cona MM, Alpizar YA, Li J, et al. Radioiodinated hypericin: its biodistribution, necrosis avidity and therapeutic efficacy are influenced by formulation. *Pharm Res* 2014;31:278–90.
 32. Liu X, Jiang C, Li Y, et al. Evaluation of hypericin: effect of aggregation on targeting biodistribution. *J Pharm Sci* 2015;104:215–22.
 33. Zhang D, Huang D, Ji Y, et al. Experimental evaluation of radioiodinated sennoside B as a necrosis-avid tracer agent. *J Drug Target* 2015;23:180–90.
 34. Motoyoshiya J, Masue Y, Nishi Y, Aoyama H. Synthesis of hypericin via emodin anthrone derived from a two-fold Diels-Alder reaction of 1, 4-benzoquinone. *Nat Prod Commun* 2007;2:67–70.
 35. Bock H, Lavie D, Mazur Y. Preparation of hypericin. Patent U.S. 5,120,412. 1992.
 36. Banks HJ, Cameron D, Raverty W. Chemistry of the Coccoidea. II. Condensed polycyclic pigments from two Australian pseudococcids (Hemiptera). *Aust J Chem* 1976;29:1509–21.
 37. Falk H, Schoppel G. On the synthesis of hypericin by oxidative trimethylemodin anthrone and emodin anthrone dimerization: isohypericin. *Monatsh Chem* 1992;123:931–8.
 38. Falk H, Schmitzberger W. On the nature of “soluble” hypericin in *Hypericum* species. *Monatsh Chem* 1992;123:731–9.
 39. Sun Z, Ni Y. Iodogen method for preparation of radioiodinated hypericin. Patent CN 200910013998. 2009.
 40. Kong M, Zhang J, Jiang C, et al. Necrosis affinity evaluation of ^{131}I -hypericin in a rat model of induced necrosis. *J Drug Target* 2013;21:604–10.
 41. Wang J, Jiang C, Jiang X, et al. The research on biodistribution of ^{131}I -iodosennoside A in normal mice and to evaluate myocardial activity. *J Isot* 2013;26:98–103.
 42. Fonge H, Van de Putte M, Huyghe D, et al. Evaluation of tumor affinity of mono- ^{123}I iodohypericin and mono- ^{123}I iodoprotohypericin in a mouse model with a RIF-1 tumor. *Contrast Media Mol Imaging* 2007;2:113–19.
 43. Bormans G, Huyghe D, Christiaen A, et al. Preparation, analysis and biodistribution in mice of iodine-123 labelled derivatives of hypericin. *J Labelled Compd Rad* 2004;47:191–8.
 44. Pietrzak M, Maciejczyk M, Szabelski M, et al. Self-association of hypericin analyzed by light absorption and fluorescence spectroscopy and molecular dynamics simulations. *Chem Phys Lett* 2014;601:39–44.
 45. Ishikawa M, Hashimoto Y. Improvement in aqueous solubility in small molecule drug discovery programs by disruption of molecular planarity and symmetry. *J Med Chem* 2011;54:1539–54.
 46. Lewin G, Maciuk A, Moncomble A, Cornard J-P. Enhancement of the water solubility of flavone glycosides by disruption of molecular planarity of the aglycone moiety. *J Nat Prod* 2012;76:8–12.
 47. Miskovsky P. Hypericin-a new antiviral and antitumor photosensitizer: mechanism of action and interaction with biological macromolecules. *Curr Drug Targets* 2002;3:55–84.

Supplementary material available online

Supplementary Data